RESEARCH ARTICLE

Efficient Photocatalytic Degradation of the Persistent PET Fiber-Based Microplastics over Pt Nanoparticles Decorated N-Doped TiO$_2$ Nanoflowers

Dawang Zhou[1] · Hongxia Luo[1] · Fangzhou Zhang[1] · Jing Wu[2] · Jianping Yang[1] · Huaping Wang[1,2]

Abstract

Fiber-based microplastics (FMPs) are highly persistent and ubiquitously exist in the wastewater of textile industry and urban sewage. It remains challenging to completely remove such newly emerged organic pollutants by the predominant physical techniques. In this work, we investigated a photocatalytic degradation catalyzed by TiO$_2$ catalyst to demonstrate the feasibility of implementing efficient chemical protocol to fast degrading polyethylene terephthalate (PET)-FMPs (a major FMP type existing in environment). The result shows that a hydrothermal pretreatment (180 °C/12 h) is necessary to induce the initial rough appearance and molecular weight reduction. With the comprehensive action of the nano-flower shaped N doped-TiO$_2$ catalyst (Pt@N-TiO$_2$-1.5%) on the relatively low molecular weight intermediates, an approximate 29% weight loss was induced on the pretreated PET-FMPs, which is about 8 times superior to the untreated sample. This work not only achieves a superior degradation effect of PET-FMPs, but also provides a new inspiration for the proposal of reduction strategies in the field of environmental remediation in the future.

Keywords Microplastics · Fiber-based microplastics · Polyethylene terephthalate · Photocatalytic degradation · Hydrothermal pretreatment

Introduction

With the continuous growth of global population and improvement of the living standards of human beings, the demand for textile products has increased sharply during the past decades [1, 2]. In 2014, the global production of fibers was 90.8 million tons (Mt), and this number is expected to increase to 130 Mt by 2025 [3]. The mass production and consumption of fiber or textiles are indispensable for the modern society, which not only satisfy the basic physical needs of humans to preserve warmth, but also meet the needs of fashion requirement and high-tech applications. Nevertheless, as a typical kind of synthetic polymer, synthetic fibers and textile products have also imposed increasingly serious environmental problems [4]. Besides the consumption of a huge amount of petrochemical energy, the waste of synthetic fiber and textile products are particularly difficult to recycle and biodegrade, as compared to other types of synthetic polymers (such as plastic films, injection-molded parts, etcs.), leading to severe waste treatment pressure to the municipal management system [5]. Currently, the majority (> 90%) of the textile waste is incinerated or landfilled, and the related environmental impacts of emitting greenhouse gases, soil and groundwater pollution is immeasurable, which is definitely a most cumbersome issue for our modern society [6].

Microplastics (MPs), which are defined as plastic particle with diameters less than 5 mm [7, 8], are a type of emerged organic pollutants realized by the scientific community in recent years. The wide presence of MPs on the earth is certainly an unexpected but highly threatening issue related to the fast development of plastic industry and improper regulation of the plastic products and/or the wastes. As one kind of

✉ Jing Wu
wuj@dhu.edu.cn

✉ Huaping Wang
wanghp@dhu.edu.cn

[1] State Key Laboratory for Modification of Chemical Fibers and Polymer Materials, College of Materials Science and Engineering, Donghua University, Shanghai 201620, China

[2] Co-Innovation Center for Textile Industry, Innovation Center for Textile Science and Technology, Donghua University, Shanghai 201620, China

MPs, fiber-based microplastics (FMPs) are different from the common perception that the typical MPs are formed evolved from the two or three-dimensional plastics films, foams or blocks, FMPs are typically featured by their one-dimensional shapes. Depending on the fiber applications, the diameters of FMPs can vary from nanometer to millimeter scale [6]. The formation of FMPs is closely related to the wearing and daily laundry of all kinds of textile products, they thus have been identified as an emerging kind of organic pollutant in the wastewater of textile industry or municipal wastewater [9–11]. FMPs are known to easily adsorb pollutants from the environment due to their high specific surface area than the large pieces of plastics, and the pollution scope can be significantly expanded as their migration in the environment [12–15]. Given their ubiquitous existence in the air, land and aquatic bodies, it is basically impossible to completely recover/collect them from the environment, or to in-situ renovate the polluted environmental medium [16–18]. The more realistic and straightforward protocol has to be that the discharge of these persistent organic pollutants into the environment can be efficiently prevented, by either physically adsorbing/blocking methods, or by chemical methods to degrade them into more valuable or harmless end-products.

There have been a few interesting works attempting to eliminate FMPs by physical or chemical strategies. Francesca et al. firstly modified pectin with glycidyl methacrylate, and then grafted them on polyamide fibers as a protective layer preventing the fibers to be abraded during the washing process. The results showed that the release of FMPs was reduced by about 90% compared with the original [19]. Although the release of FMPs had been greatly reduced, the process of preparing the composite fiber was complicated and the coating of a protective layer would affect the usability of polyamide fibers. Recently, Villa et al. reported a perovskite-like Bi_2WO_6 microrobot, which autonomously attached to the small piece of commercial wet wipes for personal cleansing and degraded them by generating active species under 50 h of sun-like irradiation [20]. This research proved that the active species with strong oxidation behavior, produced by photocatalytic technology can have a certain degradation effect on FMPs. But the degradation effect of this system is limited by only showing certain morphological and structural changes of textiles. It is therefore of vital significance to develop an efficient photocatalytic degradation technology to remove FMPs.

Titanium dioxide (TiO_2) is recognized as one of the most promising photocatalyst owning to its versatile properties, such as low-toxicity, excellent stability and relatively low cost [21–23]. By generating active species with strong oxidation behavior, such as hydroxyl radical ($^*OH$, where "*" is the active site), superoxide radical ($^*O_2^-$) and singlet oxygen ($^1O_2$), small organic contaminants can be effectively degraded or even mineralized [21]. For example,

Chen et al. synthesized an Ag/TiO_2 photocatalyst via electrospinning , by which methylene blue was degrade by 70% within 90 min [24]. Li et al. loaded the TiO_2-modified $Bi_2Ti_2O_7$ heterojunction on the surface of reduced graphene oxide to obtain a ternary photocatalytic composite material. The degradation efficiency of ciprofloxacin was 95% within 180 min [25]. It is not difficult to find that TiO_2 could destroy chemical structures and bonds such as benzene ring, C–C, and C–O by virtue of the strong oxidation behavior of active species. Although FMPs are polymer material with high molecular weight and high crystallinity, their structure still contains a large amount of C–C, C–O and other types of chemical structures and bonds. As a result, it can be inferred that it is feasible to use TiO_2 to degrade FMPs. However, their photocatalytic reaction rate is limited by the rapid recombination of photoexcited charge carriers [23, 26]. The introduction of noble metal such as aurum, silver and platinum (Pt) on the surface of TiO_2 can greatly inhibit the intention of recombination by forming a Schottky barrier [27–29]. However, another challenge that the noble metal element as the active site is easy to fall off during the photocatalytic reaction, which can make the catalytic activity of the photocatalyst decreased. Therefore, the superb catalytic performance and excellent stability are necessary for photocatalysts. Apart from the three common crystal phases of TiO_2, namely anatase, rutile and brookite, srilankite phase is known to be a transitional phase between anatase and rutile under the high pressure [30]. Due to its disordered or even amorphous structural characteristics, there are more photogenerated carrier recombination centers, which can reduce the photocatalytic activity of srilankite TiO_2 [31, 32]. But from our point of view, the existence of surface defects of uncommon srilankite TiO_2 may help anchor precious metals, thereby avoiding the decrease of photocatalytic efficiency.

In pioneering studies, N-doped TiO_2 was firstly prepared by solvothermal, and then Pt nanoparticles were loaded on the surface through the photo-deposition method. The effect of the loading of Pt nanoparticles on the photocatalytic performance and the effect of the srilankite phase on the stability of the photocatalyst were firstly analyzed in detail by degrading various contaminants, including methyl orange (MO), sodium dodecylbenzene sulfonate (SDBS), polyvinyl alcohol (PVA), dinotefuran (DTF) and tetracycline (TC). More importantly, the evaluation of the photocatalytic degradation performance of the catalytic system and identification of the active species had been completed through the above experiment. Subsequently, polyethylene terephthalate (PET) was selected as the target pollutant due to its high yield and wide range of application [33]. The weight loss was adopted to describe the degradation effect of PET-FMPs, instead of just focusing on the slight changes in its morphology and structure. Comprehensive investigations into the surface morphology, weight-average molecular

weight and crystallinity of PET-FMPs that were pretreated in different hydrothermal temperature and time, the key factors that affect the degradation effect were clarified. Finally, the photocatalytic degradation mechanism of PET-FMPs was deeply summarized. This work explores the feasibility in photocatalytic degradation of FMPs and achieves the excellent degradation performance. The outcome of this research can provide a new inspiration for the proposal of green and promising reduction strategies of FMPs and even MPs in the future.

Experimental Section

Chemicals

Isopropanol (IPA), N, N-dimethylformamide (DMF), tetrabutyl titanate (TBT), p-benzoquinone (PBQ), ethanol, polyvinyl alcohol (PVA, molecular weight ~ 27,000) and anhydrous sodium sulfate (Na_2SO_4) were purchased from Sinopharm Chemical Reagent Co., Ltd. L-histidine, ammonium oxalate monohydrate (AO), methyl orange (MO), sodium dodecylbenzene sulfonate (SDBS), dinotefuran (DTF), tetracycline (TC), commercial TiO_2 (P25), pure anatase phase TiO_2 (A-TiO_2), 1-naphthol and chloroplatinic acid hexahydrate ($H_2PtCl_6 \bullet 6H_2O$) were purchased from Shanghai Macklin Biochemical Technology Co., Ltd. PET fibers were obtained by Ningbo Dafa Chemical Fiber Co., Ltd. FTO glasses (20×10 mm resistance: 14 Ohm) were purchased from Luoyang Guluo Glass Co., Ltd.

Synthesis of N-TiO$_2$

N-doped TiO_2 was synthesized with some modifications according to the synthetic protocol step supplied in the reference [34]. Briefly, 30 mL IPA was mixed with 10 mL DMF for 10 min, and then 1 mL TBT was added to the mixture. The mixture was stirred for another 10 min and subsequently transferred into a 60-mL Teflon-lined stainless-steel autoclave and kept in an electric oven at 200 °C for 24 h. The product was collected by centrifugation after being cooled to room temperature, washed again with ethanol for 3–5 times and dried overnight. Finally, the as-prepared product was placed in the muffle furnace, and calcined in air at 450 °C for 2 h at a heating rate of 5 °C/min to obtain the N-doped TiO_2 (N-TiO_2).

Synthesis of Pt@N-TiO$_2$-x

N-doped TiO_2 nanoflowers decorated with Pt nanoparticles (Pt@N-TiO_2-x, x means the varied Pt loadings) were prepared through the photo-deposition method.

100 mg N-doped TiO_2 was dispersed in 80 mL of deionized water containing a certain amount of $H_2PtCl_6 \bullet 6H_2O$ solution (4 g/L) under magnetic stirring for 1 h. Afterwards, the dispersion was irradiated under 300 W Xenon lamp with a light filter of 420 nm. The sample was collected by centrifugation, washed with deionized water and ethanol for 3–5 times respectively, and dried at 60 °C to obtain the final product. The amount of Pt loading in the N-doped TiO_2 matrix was adjusted by changing the volume of the added $H_2PtCl_6 \bullet 6H_2O$ solution.

Synthesis of Pt@P25

N-TiO_2 was replaced by P25 as the matrix supported by Pt nanoparticles and the remaining operation steps and reagent dosage were consistent with the Pt@N-TiO_2-x synthesis method to obtain the Pt@P25 as a comparison.

Synthesis of Pt@A-TiO$_2$

Using A-TiO_2 instead of N-TiO_2 as the substrate for Pt nanoparticles, the operation steps and the amount of reagents were consistent with the Pt@N-TiO_2-x synthesis method, and Pt@A-TiO_2 was obtained as a comparison.

Characterization

X-ray diffractometer (XRD) was analyzed with Bruker D2 Phaser. Scanning electron microscope (SEM) was performed by TESCAN/MAIA3, Czech. Transmission electron microscopy (TEM) images and elemental mapping analysis were collected by using Talos F200S. X ray photoelectron spectroscopy (XPS) and valence-band spectra was carried out on the Thermo ESCLAB 250Xi. Electron paramagnetic resonance (EPR) analysis were conducted at room temperature using the A300-10/12. 5,5-dimethyl-1-pyrrolidine-N-oxide (DMPO) and 4-oxo-2,2,6,6-tetra methylpiperidine (TEMPO) was adopted as the spin-trapping agent to conduct an ESR analysis. Nitrogen adsorption–desorption isotherms were analyzed on Quantachrome instruments. The BET (Brunauer–Emmett–Teller) was employed to calculate the specific surface area. The Barrett–Joyner–Halenda (BJH) was utilized to estimate pore size distributions according to the adsorption isotherm. The diffuse reflectance spectroscopy (DRS) performed on a UV–vis spectrophotometer (UV-3600 (Japan SHIMADZU)) in the range of 350–700 nm with fine $BaSO_4$ powders as reference. The photoluminescence (PL) spectrum was obtained via FLS1000/FS5 Edinburgh instruments. The photocurrent-time (I-t) and electrochemical impedance spectroscopy (EIS) were measured by the electrochemical workstation (CHI-660E). The total organic carbon (TOC) was analyzed by a TOC measuring

instrument on Muti N/C 2100. Some important intermediates in degradation reaction were tested on a gas chromatography- Mass spectrometry GC–MS (QP2010Ultra). Gel permeation chromatography (GPC) was determined on a GPC-50 (polymer Laborato). Differential scanning calorimetry (DSC) were recorded from 30 to 280 °C on a DSC 214 (NETZSCH). Inductive Coupled Plasma Emission Spectrometer (ICP) was conducted on Prodigy-ICP. Fourier Transform Infrared Spectrometer- Attenuated Total Reflection (FTIR- ATR) was performed on */NEXUS-670 in the range of 650–4000 cm^{-1}.

Photocatalytic degradation tests

Photocatalytic degradation tests of various contaminants

The photocatalytic activity of the catalysts was evaluated by degrading various contaminants, including MO, SDBS, PVA, DTF and TC. A 300 W Xe lamp equipped with AM 1.5 filter was employed as the light source, and the irradiation intensity was regulated as 100 mW/cm^2. A typical degradation experiment was illustrated by using MO: 20 mg of the photocatalyst was dispersed in 100 mL MO solution (10 mg/L), under ultrasonic treatment. To eliminate the influence of physical adsorption, the suspension was stirred for 10 min in the dark to achieve adsorption–desorption equilibrium. Then, the suspension was irradiated under intense agitation, took 6 mL solution once per 5 min, and filtered through 0.22 μm Millipore filters in order to get rid of the catalysts. The resulting solution was analyzed by UV spectrophotometer at 465 nm, which is the wavelength of the UV absorption of MO. According to Lambert–Beer law, the photocatalytic degradation efficiency of MO was calculated as follows:

$$\text{Photocatalytic degradation efficiency} = \frac{C_0 - C_t}{C_0} \times 100\% \quad (1)$$

where C_0 (mg/L) and C_t (mg/L) represent the initial MO concentration and instantaneous MO concentration after a certain irradiation time (t), respectively.

TOC analysis was used to determine the change of the content of total organic carbon in the system before and after degradation. Similarly, the taken solution of all contaminants, including MO, SDBS, PVA, DTF and TC was analyzed by TOC, the TOC removal efficiency was calculated as follows:

$$\text{TOC removal efficiency} = \frac{TOC_0 - TOC_{30\,min}}{TOC_0} \times 100\% \quad (2)$$

where TOC_0 (mg/L) and $TOC_{30\,min}$ (mg/L) represent the initial TOC content of the pollutant and instantaneous TOC content of the pollutant after the irradiation time of 30 min, respectively.

In order to verify the cycle stability of the photocatalyst, the recovered photocatalyst was washed with deionized water and ethanol for 3–5 times to remove the degradation residuals and then the adsorption and photocatalytic degradation tests were repeated as above indicated.

Photocatalytic Degradation Tests of PET-FMPs

PET-based FMPs (PET-FMPs) were obtained by directly cutting PET fibers (diameter ~ 25 μm) into lengths smaller than 5 mm. The same type of light source was used in this case with comparable irradiation intensity as for the degradation of various contaminants, while a few modifications have been made in some operation steps. Specifically, 20 mg of the photocatalyst was dispersed in a suspension of PET-FMPs (100 mg/L) by assisting with ultrasound. Subsequently, the suspension was stirred in the dark for 10 min to reach adsorption equilibrium, which was exposed under the intense irradiation for 48 h. After experiments, a solid mixture of photocatalyst and PET-FMPs was collected by suction with 0.10 μm filter membrane and cleaned for 3–5 times by deionized water, and then dried at 60 °C for 24 h. The filtrate was analyzed by GC–MS to determine the composition of liquid product. The weight loss of the PET-FMPs was calculated as follows:

$$\text{Weight loss} = \frac{M_0 - M_{48\,h}}{M_0} \times 100\% \quad (3)$$

where M_0 (mg) and $M_{48\,h}$ (mg) represent the initial total mass of the filter membrane, photocatalysts and PET-FMPs before and after irradiation for 48 h. All the degradation test of PET-FMPs was repeated for three times and the mean values and standard deviation of weight loss are presented.

Photoelectrochemical Property Test of Photocatalysts

Characterization of the photoelectrochemical properties of photocatalysts were conducted by using CHI-660E electrochemical station. In a three-electrode quartz cell, the electrolyte solution was 0.5 M Na$_2$SO$_4$, Ag/AgCl and a Pt wire were applied as the reference electrode and the counter electrode, respectively, and N-TiO$_2$ and Pt@N-TiO$_2$-1.5% were used as the photoanodes. The photoanode was prepared by a simple physical coating process. 5 mg of photocatalyst was ultrasonically dispersed in the mixture of 20 μL 1-naphthol and 500 μL ethanol, which was evenly coated on the FTO glass, and then dried at 60 °C for 24 h.
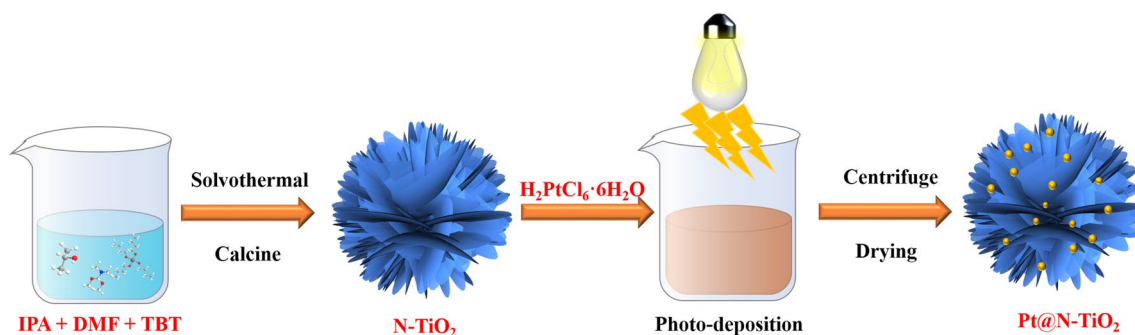
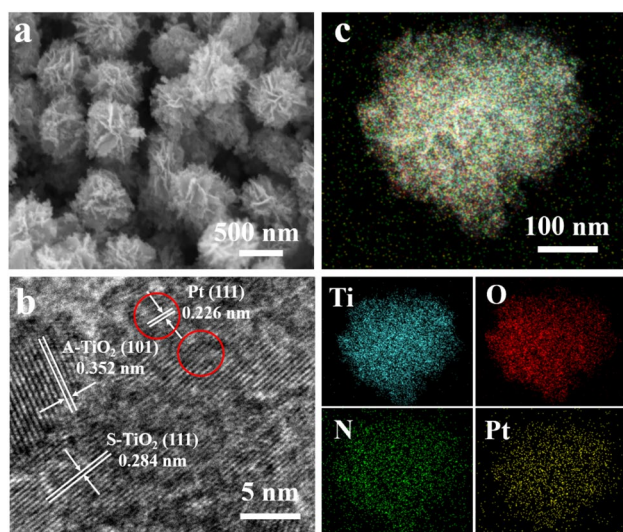**Fig. 1** Schematic diagram of the synthesis procedure of Pt@N-TiO$_2$

Fig. 2 **a** SEM image, **b** HRTEM image and **c** EDS elemental mappings of Pt@N-TiO$_2$-1.5%

Fig. 3 **a** XRD patterns of N-TiO$_2$ and Pt@N-TiO$_2$-x. **b** XPS survey spectra and **c** EPR spectra of Pt@N-TiO$_2$-1.5%. **d** Nitrogen adsorption–desorption isotherm curve of N-TiO$_2$ and Pt@N-TiO$_2$-1.5%

Results and Discussion

Morphology and Structure Analysis of Photocatalysts

The synthetic process of the photocatalysts was elucidated in Fig. 1. In brief, the matrix of N-TiO$_2$ was firstly prepared by solvothermal, and then Pt nanoparticles were decorated on its surface through a photo-deposition method.

As shown in SEM and TEM images (Supporting Information, Fig. S1, Fig. 2a), N-TiO$_2$ and Pt@N-TiO$_2$-1.5% had a unique nanoflower structure, which was expected to be beneficial to facilitate the reflection of light among the surface nanosheets, thereby enhancing the sunlight absorption capacity and improving the photocatalytic performance [34]. Their particles were uniform and the size was about 500 nm. The HRTEM image shows that a lattice
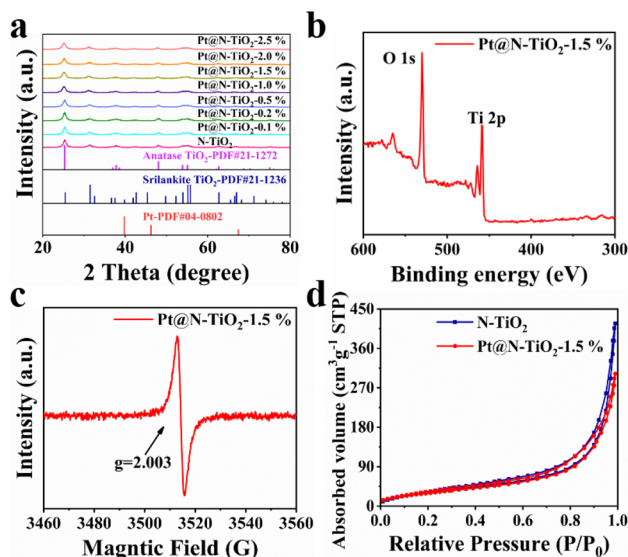
spacing of 0.352 nm and 0.284 nm corresponding to the (101) and (111) planes, which were indexed as the antase (A)-TiO$_2$ and srilankite (S)-TiO$_2$, respectively (Fig. 2b). It indicated that the N-TiO$_2$ was a mixture of anatase and srilankite. The Pt nanoparticles are perfectly crystallized with a lattice spacing of 0.226 nm corresponding to the (111) planes of crystalline Pt (particle size ~ 5 nm). EDS elemental mappings were employed to identify the composition of elements in the composite. As shown in Fig. 2c, it was clearly observed that Ti, O, N, and Pt were uniformly distributed on the entire structure. These results demonstrated that Pt nanoparticles were successfully united in wedlock on the nanoflowers.

The crystalline structure of N-TiO$_2$ and Pt@N-TiO$_2$-x was analyzed by XRD. As shown in Fig. 3a, the crystalline structure of TiO$_2$ remained unchanged after deposition of Pt nanoparticles. No Pt peaks were observed in XRD due to their

extremely small size and low dosage [35, 36]. Moreover, it could further demonstrate that the N-TiO$_2$ was composed of anatase and srilankite. XPS survey spectra was employed to reveal the surface chemical state of the Pt@N-TiO$_2$-1.5%. Figure 3b showed the full spectra of Pt@N-TiO$_2$-1.5%, there were only O 1s, Ti 2p and C 1s speaks were observed owing to the low content of Pt and N. C 1s peak was ascribed to the adsorption of carbon dioxide (CO$_2$) from the environment during sample preparation [28]. Pt 4f, N 1s, Ti 2p and O 1s peaks could be clearly presented in their high-resolution spectra (Supporting Information, Fig. S2 and S3). The peak located at 400.1 eV was indexed to the Ti–O-N [37]. The binding energy of 458.0 eV and 463.7 eV were assigned to Ti 2p$_{3/2}$ and Ti 2p$_{1/2}$ respectively. The chemical shift of 5.7 eV proved that the chemical state of Ti was Ti^{4+} [38]. In addition, the g value of 2.003 was observed in the EPR spectra of N-TiO$_2$ and Pt@N-TiO$_2$-1.5%, which was ascribed to the Zeeman effect of single electron [39–41], demonstrating the formation of oxygen vacancies (Fig. 3c) and the deposition of Pt nanoparticles did not affect their existence (Supporting Information, Figure S4) [42]. Notably, the photocatalytic performance might be improved with the help of oxygen vacancies, because they could temporarily trap electrons to prolong the lifetime of carriers [43]. By examining the nitrogen adsorption–desorption isotherms, the corresponding pore structure information of N-TiO$_2$ and Pt@N-TiO$_2$-1.5% (Fig. 3d and Supporting Information, Table S1) were obtained. Both curves displayed a typical IV isotherms with H3 typical hysteresis loop, indicating that these two photocatalysts have the mesoporous structure, which was beneficial for the diffusion of reactants and products [44]. There was an obvious deviation between the values of their surface area, average pore size and pore volume, further demonstrating the efficient loading of Pt nanoparticles.

UV–vis DRS spectra was utilized to analyze the optical absorption properties of the N-TiO$_2$ and Pt@N-TiO$_2$-1.5%. As revealed in Fig. 4a, a slight red-shifted of adsorption edge toward visible region was found in the Pt@N-TiO$_2$-1.5%. It implied that the deposition of Pt nanoparticle leaded to an increase of light absorption in the visible light region, which
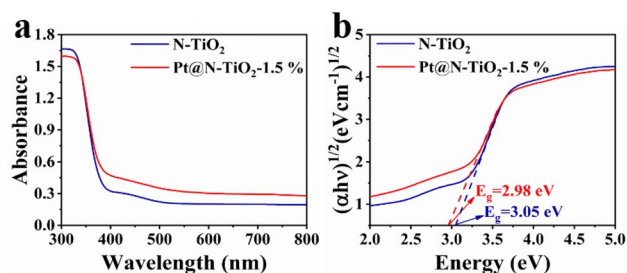
was conductive to enhancing the practical application potential of photocatalyst. Additionally, the bandgap of the photocatalyst could be calculated according to the Kubelka–Munk function equation: $(\alpha h\upsilon)^{1/2} = K(h\upsilon - E_g)$ for the direct bandgap (where "α"is the absorption index,"$h\upsilon$" is the light energy, "K" is a constant value and "E_g" is the bandgap energy) [45]. The corresponding function transformed differential spectra was shown in Fig. 4b. By extrapolating the linear region of the square root of absorbance versus energy, the bandgap energy of Pt@N-TiO$_2$-1.5% was estimated to be 2.98 eV, which was less than that of N-TiO$_2$ (3.05 eV).

Photocatalytic Degradation of the Various Chemical Additives and Contaminants

As observed from Fig. 5a, the photocatalytic degradation efficiency of MO for Pt@N-TiO$_2$-1.5% was remarkably high of 95.88% within 30 min, achieving almost complete degradation and its performance was much higher than that of N-TiO$_2$. On the other hand, the linear relation of -ln (C_t/C_0) for N-TiO$_2$ and Pt@N-TiO$_2$-1.5% could be acquired and the linear trend demonstrated that the photocatalytic degradation process of MO was fitted well with pseudo-first-order
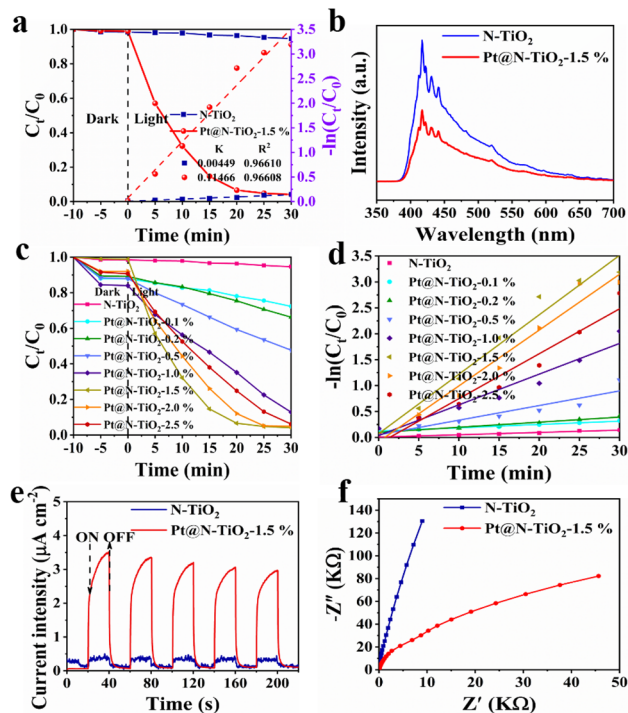
Fig. 5 a Photocatalytic degradation efficiency of MO and the corresponding variations in -ln (C_t/C_0) of N-TiO$_2$ and Pt@N-TiO$_2$-1.5% under AM 1.5 irradiation. **b** PL spectra of N-TiO$_2$ and Pt@N-TiO$_2$-1.5%. **c** Photocatalytic degradation efficiency of MO and **d** the corresponding variations in -ln (C_t/C_0) of N-TiO$_2$ with different loading amounts of Pt nanoparticles under AM 1.5 irradiation. **e** I-t and **f** EIS curves of N-TiO$_2$ and Pt@N-TiO$_2$-1.5%

Fig. 4 a UV–vis DRS spectra, and **b** the corresponding plots of $(\alpha h\upsilon)^{1/2}$ versus hυ of N-TiO$_2$ and Pt@N-TiO$_2$-1.5%

kinetics. Furthermore, the Pt@N-TiO$_2$-1.5% had the highest degradation rate constant (k = 0.11466 min^{-1}), which was about 25 times higher than that of N-TiO$_2$ (k = 0.00449 min^{-1}). We speculated that such a superior photocatalytic activity of Pt@N-TiO$_2$-1.5% was attributed to the better photo-generated electron–hole pairs separation efficiency due to the formation of a Schottky barrier at the interface between the Pt nanoparticles and the matrix of N-TiO$_2$. Therefore, we further analyzed the photogenerated carrier separation efficiency of the photocatalysts by PL spectra. As shown in Fig. 5b, the PL intensity of Pt@N-TiO$_2$-1.5% was lower than that of N-TiO$_2$, demonstrating the fast separation of the photogenerated carrier with the presence of Pt nanoparticles. The photocatalytic degradation efficiency of MO for Pt@N-TiO$_2$-x with different loading amounts of Pt nanoparticles was conducted. As shown in Fig. 5c, d, with the increase of Pt nanoparticles, the photocatalytic degradation efficiency and k increased firstly and then decreased, and the highest photocatalytic degradation performance was achieved with the loading amount of Pt nanoparticles of 1.5%. It indicated that the appropriate amount of Pt nanoparticles on the surface of N-TiO$_2$ could play an important role in inhibiting the recombination of carriers by building a Schottky barrier at the material interface. However, Pt nanoparticles tended to aggregate when overloaded, which might reduce the number of effective active sites, resulting in a decrease in photocatalytic performance [46]. I-t curves of N-TiO$_2$ and Pt@N-TiO$_2$-1.5% were recorded by the intermittent irradiation for several switching cycles under AM 1.5 irradiation. As observed from Fig. 5e, the Pt@N-TiO$_2$-1.5% obtained a higher photocurrent density, which demonstrated that the photoresponse performance of N-TiO$_2$ was improved after Pt nanoparticles loading. In addition, as exhibited in Fig. 5f, the EIS Nyquist diagrams were used to characterize the capacity of charge transfer between the electrode interfaces. Obviously, the arc radius of Pt@N-TiO$_2$-1.5% in the EIS Nyquist plot was smaller than that of N-TiO$_2$, implying that Pt@N-TiO$_2$-1.5% had better conductivity.

As presented in Fig. S5a (Supporting Information), the photocatalytic degradation efficiency of MO nearly kept constant after 5 cycles of consecutive photocatalytic reaction. Based on a further XRD analysis, no significant change was noticed for the fresh and used Pt@N-TiO$_2$-1.5%, revealing its stable crystalline structure (Supporting Information, Figure S5b). As a comparison, the photocatalytic degradation efficiency of MO for Pt@A-TiO$_2$-1.5% and Pt@P25-1.5% decreased obviously after only 3 cycles of degradation reaction (Supporting Information, Fig. S5c). TOC (total organic carbon) removal efficiency of MO was as high as 56.85% within 30 min, suggesting that the photocatalyst not only had outstanding photocatalytic degradation performance, but also its mineralization capacity was also remarkable. Except MO, several other common contaminants had also

been investigated under the same experimental conditions, including SDBS PVA, DTF and TC. TOC removal efficiency of all these contaminants were in a range of 40–50% within 30 min (Supporting Information, Fig. S5d). The above result suggested that Pt@N-TiO$_2$-1.5% had an outstanding catalytic stability, which was mainly due to the existence of srilankite phase. It could effectively inhibit the loss of active sites relying on its surface defects to firmly anchor Pt nanoparticles during the multiple cycles.

There are two ways to effectively identify the active species, for exploring the degradation mechanism; Direct method is based on using ESR technology in combination with trapping agent to capture active species, and indirect method utilizes the quenching agents to inhibit the catalytic activity of the active species, and the existence of active species can be confirmed when the degradation efficiency is reduced. In this work, ESR analysis was firstly employed to determine the active species produced by Pt@N-TiO$_2$-1.5% under light and dark conditions. In Fig. 6a–c, the characteristic signals of the DMPO-the superoxide radical ($^*O_2^-$), TEMPO-the singlet oxygen ($^1O_2$) and
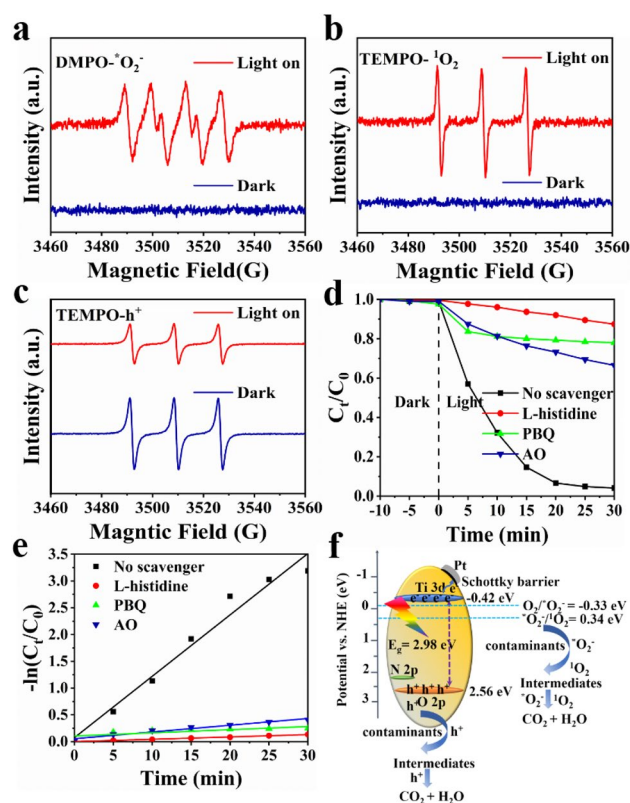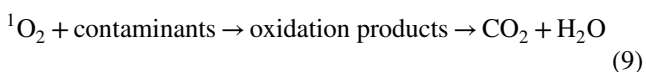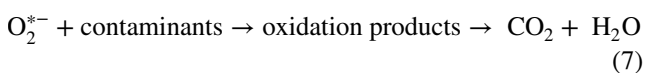

Fig. 6 ESR signals of (**a**) DMPO-$^*O_2^-$, (**b**) TEMPO-$^1O_2$, and (**c**) TEMPO-h$^+$ of Pt@N-TiO$_2$-1.5% in the dark and under AM 1.5 irradiation. **d** Photocatalytic degradation efficiency of MO and (**e**) the corresponding variations in -ln (C$_t$/C$_0$) of Pt@N-TiO$_2$-1.5% in the presence of different scavengers under AM 1.5 irradiation. **f** Degradation mechanism of contaminants of Pt@N-TiO$_2$-1.5% under AM 1.5 irradiation

TEMPO-the photon-generated hole (h^+) were detected. Additionally, a series of quenching experiments were performed by using p-benzoquinone (PBQ), L-Histidine and ammonium oxalate monohydrate (AO) as the scavenger for $^*O_2^-$, $^1O_2$ and h^+, respectively. As shown in Fig. 6d–e, the photocatalytic degradation efficiency and k significantly reduced when the scavenger was added to the reaction. Based on the above experimental results, it could be determined that $^*O_2^-$, $^1O_2$ and h^+ as the main active species participated in the degradation of contaminants during the photocatalytic reaction.

According to the XPS spectra of Pt@N-TiO$_2$-1.5%, the maximum valence-band of this catalyst was 2.56 eV (Supporting Information, Fig. S6). The corresponding band structure was established by simultaneously considering the bandgap energy (2.98 eV), and the photocatalytic degradation mechanism was proposed in Fig. 6f. Specifically, the conduction-band edge potential of Pt@N-TiO$_2$-1.5% was more negative than that of $O_2/^*O_2^-$ pair (− 0.33 eV vs NHE, where "eV" is the unit of voltage, and "NHE" is the normal hydrogen electrode) [47], and its valence-band edge potential was more positive than the potential of $^*O_2^-/^1O_2$ pair (0.34 eV vs NHE) [22]. Consequently, the outstanding photocatalytic degradation ability of the reaction system mainly depended on the combined action of the three active species ($^*O_2^-$, $^1O_2$ and h^+). Firstly, the optical energy was absorbed by the photocatalyst so that electrons (e^-) in the valence band (VB) were excited to the conduction band (CB), then h^+ were created in the VB under the irradiation (Eq. 4). Since h^+ had a certain oxidation capacity, it could directly adsorb and degrade contaminants. In addition, e^- reacted with oxygen in the system to form $^*O_2^-$ (Eq. 6), which were further partially oxidized to form $^1O_2$ (Eq. 8). Contaminants were gradually degraded and finally mineralized into CO$_2$ and water (H$_2$O) under the continuous attack of the three active species (Eq. 5, 7, 9). Both the radical pathway and non-radical pathway contributed to the effective decomposition of contaminants.

$$Photocatalyst + h\nu \rightarrow h^+ + e^- \tag{4}$$

$$h^+ + contaminants \rightarrow oxidation\ products \rightarrow CO_2 + H_2O \tag{5}$$

$$e^- + O_2 \rightarrow O_2^{*-} \tag{6}$$

$$O_2^{*-} + contaminants \rightarrow oxidation\ products \rightarrow CO_2 + H_2O \tag{7}$$

$$O_2^{*-} \rightarrow {}^1O_2 \tag{8}$$

$$^1O_2 + contaminants \rightarrow oxidation\ products \rightarrow CO_2 + H_2O \tag{9}$$
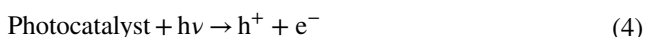
Photocatalytic Degradation of PET-FMPs

Evaluation of the photocatalytic performance of the catalytic system and the identification of the active species has been so far implemented by applying them for various contaminants. Since PET is currently the largest and most widely used synthetic fiber in the world [48], we chose PET-FMPs as a contaminant model of FMPs to investigate the degradation performance of our photocatalysts. As shown in Fig. 7a, the surface of untreated PET-FMPs was relatively smooth with neat fiber edges and no deformation before photocatalytic degradation. After 48 h of direct exposure under AM 1.5 irradiation without photocatalyst added, a few cracks and spots on the untreated PET-FMPs could be observed (Fig. 7b), while the weight loss was almost negligible ($1.51 \pm 0.74\%$, Fig. 8a). When the photocatalyst (Pt@N-TiO$_2$-1.5%) was present, it was interesting to notice that the morphology of untreated PET-FMPs drastically changed. Most of the PET-FMPs became the sheet-like structure, and the surface of the residual fibers became rougher (Fig. 7c). The weight loss of this case was slightly increased compared to the original, but it remains very low ($5.83 \pm 0.82\%$) (Fig. 8a). It indicated that relying solely on the active species generated in the system was not effective enough to decompose the highly persistent PET-FMPs. Compared to common contaminants, polymer properties including high molecular weight, high crystallinity, and strong intermolecular forces make PET-FMPs become a highly resistant material. Based on the above results, the pretreatment might be carried out on PET-FMPs to make great changes in polymer properties so that it is easier to be degraded by active species. Hence, the hydrothermal pretreatment was firstly performed on PET-FMPs, and then the photocatalytic degradation technology was utilized to degrade them.

As shown in Fig. 7d, PET-FMPs transformed into a short rod-like structure with thin flakes neatly arranged on the surface after a hydrothermal pretreatment at 180 °C for 12 h. When it was exposed to light without photocatalyst added, it was obvious that the length of these rods became shorter and the rod-like structure was much more irregular or even completely collapsed into small particles (Fig. 7e). Once Pt@N-TiO$_2$-1.5% was added to the system, the short rod-like structure of the pretreated PET-FMPs was destroyed completely and the morphology of the product was similar to that of the molten polymer at this time (Fig. 7f). The morphological and structural changes were more significant than that of untreated PET-FMPs under the same degradation conditions. It is worth noting that in the absence or presence of the Pt@N-TiO$_2$-1.5%, the weight loss has been increased to $3.70 \pm 1.13\%$ and $28.96 \pm 2.59\%$, respectively (Fig. 8a). The above experimental results confirmed that the
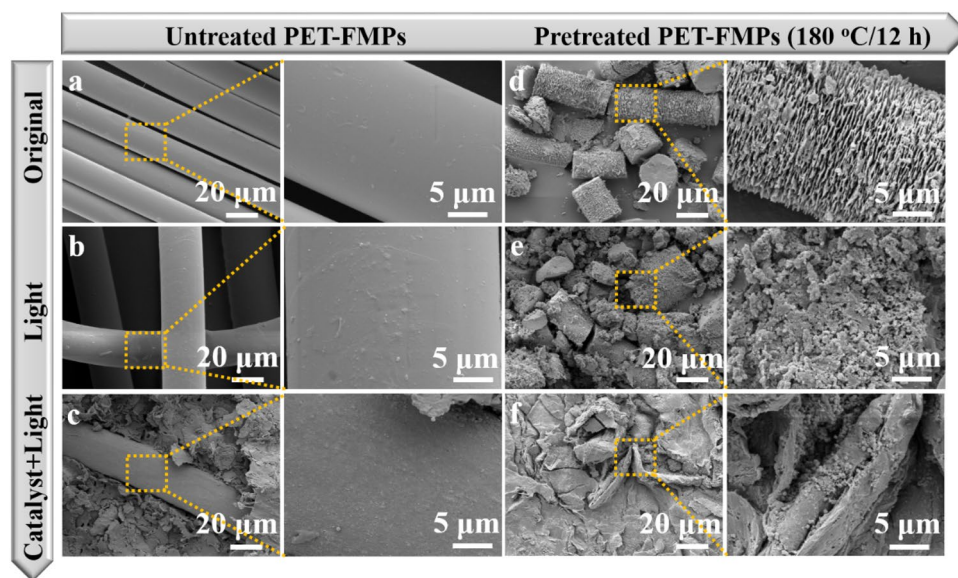
Fig. 7 SEM image and the corresponding partial enlarged image of (**a**) untreated PET-FMPs and (**d**) pretreated PET-FMPs by hydrothermal (180 °C/12 h) before photocatalytic degradation. SEM image and the corresponding partial enlarged image of (**b**) untreated PET-FMPs and (**e**) pretreated PET-FMPs by hydrothermal (180 °C/12 h) without Pt@N-TiO$_2$-1.5% added after photocatalytic degradation under AM 1.5 irradiation. SEM image and the corresponding partial enlarged image of (**c**) untreated PET-FMPs and (**f**) pretreated PET-FMPs by hydrothermal (180 °C/12 h) with Pt@N-TiO$_2$-1.5% added after photocatalytic degradation under AM 1.5 irradiation

Fig. 8 a Weight loss of untreated PET-FMPs without Pt@N-TiO$_2$-1.5% added, untreated PET-FMPs with Pt@N-TiO$_2$-1.5% added, pretreated PET-FMPs by hydrothermal (180 °C/12 h) without Pt@N-TiO$_2$-1.5% added and pretreated PET-FMPs by hydrothermal (180 °C/12 h) with Pt@N-TiO$_2$-1.5% add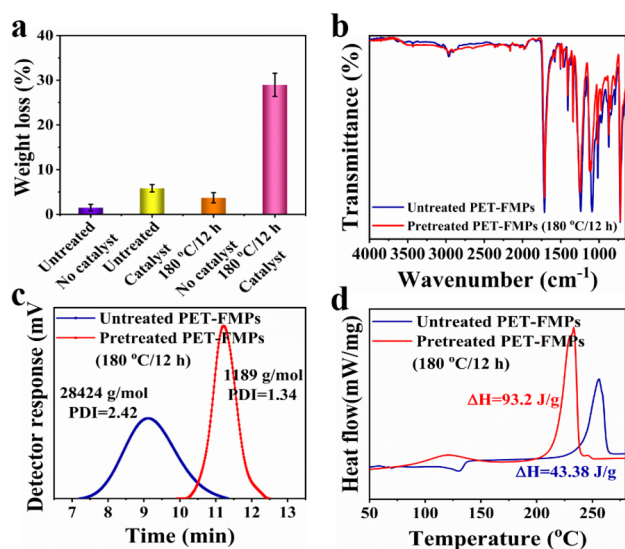ed after photocatalytic degradation under AM 1.5 irradiation. **b** FTIR-ATR spectrum, **c** GPC analysis and **d** DSC analysis of untreated PET-FMPs and pretreated PET-FMPs by hydrothermal (180 °C/12 h)

pretreated PET-FMPs were indeed beneficial to the attack of active species, thus obtaining a high weight loss.

As mentioned before, the pretreated PET-FMPs completely lost their original smooth fibrous structure, the tightly arranged sheet enhanced the effective contact with the photocatalyst by increasing the specific surface area, and the gap between the sheets could facilitate the penetration of the photocatalysts, thereby attacking the inside of the PET-FMPs more effectively not just the surface damage. As shown in Fig. 7f, a large amount of photocatalysts adhered to the solid residues of the PET-FMPs after photocatalytic degradation, while the photocatalyst was almost invisible in the untreated PET-FMPs degradation residues (Fig. 7c), which demonstrated the correctness of the above speculation. In addition, there was almost no chemical shift in the peak position of the group in PET-FMPs, but the corresponding transmittances all presented a certain reduction in the FTIR-ATR spectra (Fig. 8b). It implied that the internal structure of the PET-FMPs might have changed after hydrothermal pretreatment. GPC was used to analyze the changes in the weight-average molecular weight of PET-FMPs before and after pretreatment. As exhibited in Fig. 8c, the weight-average molecular weight of PET-FMPs had dropped sharply from 28424 g/mol to 1189 g/mol. It is well known that the molecular weight of a polymer is a quantitative parameter of

molecular chain length [14]. Therefore, the molecular chain in the pretreated PET-FMPs was cut and became shortened, which could help active species to attack and decompose them more effectively. As shown in Fig. 8d, the change in the crystallinity of PET-FMPs could be calculated based on the thermal information analyzed by DSC using the equation: $X_c = \Delta H / \Delta H_0 = \Delta(H_m - H_c) / \Delta H_0$ (where "X_c" is the crystallinity, "ΔH_m" is the fusion enthalpy, "ΔH_c" is the crystallization enthalpy and "ΔH_0" is the enthalpy of complete fusion (140 J/g). To our surprise, the crystallinity of the pretreated PET-FMPs increased from the initial 30.99% to 66.57%. The possible reason for this phenomenon was that PET-FMPs is a semi-crystalline polymer, and the amorphous part was easier to be degraded under the action of heat and fell off, while the thermal degradation of the crystalline part was relatively more difficult because of a higher crystallinity [5]. As a result, the proportion of the crystalline part had been greatly increased compared with the original, thereby increasing the crystallinity. In addition, the close-packed layered structure formed on the surface of the pretreated PET-FMPs might also originate from the partial degradation of amorphous part. Notably, although the weight loss of pretreated PET-FMPs can be increased to $28.96 \pm 2.59\%$, unlike the sharp changes in morphology and weight-average molecular weight that played a positive role in promoting photocatalytic degradation, the increase in crystallinity might be the key factor that limited the increasing of weight loss. Specifically, the substantial increase in crystallinity manifested that the internal molecular chain arrangement of PET-FMPs was more orderly, which could enhance the interaction between the molecular chains [8]. It was not conducive to the attack of active species, thereby hindering the progress of photocatalytic degradation.

In order to further determine the factors affecting the photocatalytic degradation of FMPs, the influence of different hydrothermal temperature and time on its weight loss was investigated. As presented in Fig. S7a (Supporting Information), it was clearly found that the weight loss of the PET-FMPs gradually increased with temperature increasing, and the same phenomenon also was observed in the accumulation of time (Supporting Information, Fig. S7b). The morphology, weight-average molecular weight and crystallinity of PET-FMPs after hydrothermal pretreatment at different temperature and time were detected.

It could be seen from the surface morphology of PET-FMPs did not change significantly when pretreated at lower temperatures (60–140 °C) for even 12 h (Supporting Information, Fig. S8a–c). In contrast, at 180 °C for only 4 h, it was observed that the roughness of PET-FMPs increased dramatically. (Supporting Information, Fig. S8d). As the hydrothermal treatment was prolonged to 8 h, a large number of holes were noticed to form on the surface of the fibers (Supporting Information, Fig S8e). The degree of change in the surface morphology of PET-FMPs was positively correlated with its weight loss. On the other hand, the weight-average molecular weight and crystallinity of PET-FMPs at different hydrothermal temperature and time were also analyzed, and the variation tendency of weight-average molecular weight was also consistent with the change trend of weight loss (Supporting Information, Fig. S7c), while the change of crystallinity was opposite (Supporting Information, Fig. S7d). Overall, it could be concluded that the rough morphology and the reduction of weight-average molecular weight were indeed beneficial to the photocatalytic degradation of PET-FMPs, while the increase in crystallinity was the limited factor hindering the improvement of weight loss.

In addition, the degradation intermediates of PET-FMPs were further analyzed by GC–MS, and a total of 13 short-chain substances were detected. The molecular formula and structure of each product were recorded in Table 1. The identified substances included alcohols, carboxylic acids, aldehydes, esters and olefins. The photocatalytic degradation of PET-FMPs by Pt@N-TiO$_2$-1.5% depended on the generation of active species, including $^*O_2^-$, $^1O_2$ and h$^+$, and a possible degradation mechanism was proposed as follows. Firstly, the transfer of h$^+$ from Pt@N-TiO$_2$-1.5% to PET-FMPs could weaken C–C bond of their molecular structure, and eventually mineralized them into CO_2 [49]. Meanwhile, PET-FMPs were directly oxidized by $^*O_2^-$ and $^1O_2$ to form organics containing oxygen groups, and fell off into the solution together with organic intermediates. Then, these degradation intermediates continued to be oxidized and degraded into smaller fragments with low molecular weight such as alcohols, carboxylic acids, and aldehydes. Ultimately, these substances were partially mineralized into CO_2 and H_2O [50–52].

Conclusions

In conclusion, we have achieved a superior degradation effect of PET-FMPs ($28.96 \pm 2.59\%$) by the generated active species ($^*O_2^-$, $^1O_2$ and h$^+$) by assisting with hydrothermal pretreatment. The result shows that a hydrothermal pretreatment (180 °C/12 h) is necessary to induce the initial rough appearance and molecular weight reduction, which are the positive factors affecting the photocatalytic degradation effect of PET-FMPs. To be specific, the sheet-like structure closely arranged on the surface of pretreated PET-FMPs, which was beneficial to increase the contact with the photocatalyst and attack the inside of the PET-FMPs more effectively not just the surface damage. Moreover, the decrease in the weight-average molecular weight of PET-FMPs means that the molecular chain becomes shorter, which is more conducive to the attack of active species. However, the increased crystallinity of pretreated PET-FMPs

Table 1 Intermediates formed upon Pt@N-TiO$_2$-1.5% photocatalytic degradation of PET-FMPs, identified by GC–MS analysis

Compound	Structure	Molecular formula	Molecular mass
1,3-Cyclopentadiene,5-(1-methylethylidene)		C$_8$H$_{10}$	106
2-Heptanone, 4,6-dimethyl		C$_9$H$_{18}$O	142
Ethanol, 2-(octyloxy)		C$_{10}$H$_{22}$O$_2$	174
Benzene, 1,3-bis(1,1-dimethylethyl)		C$_{14}$H$_{22}$	190
Benzaldehyde, 4-propyl		C$_{10}$H$_{12}$O	148
Phenol, 2,4-bis(1,1-dimethylethyl)		C$_{14}$H$_{22}$O	206
Dodecanoic acid		C$_{12}$H$_{24}$O$_2$	200
Hexamethylene diacrylate		C$_{12}$H$_{18}$O$_4$	226
Propanoic acid, 2-methyl-, 1-(1,1-dimethylethyl)-2-methyl-1,3-propanediyl ester		C$_{16}$H$_{30}$O$_4$	286
Heneicosane		C$_{21}$H$_{44}$	296
1,2-Benzenedicarboxylic acid, bis(2-methylpropyl) ester		C$_{16}$H$_{22}$O$_4$	278
7,9-Di-tert-butyl-1-oxaspiro(4,5)deca-6,9-diene-2,8-dione		C$_{17}$H$_{24}$O$_3$	276
l-(+)-Ascorbic acid 2,6-dihexadecanoate		C$_{38}$H$_{68}$O$_8$	652

indicates that its internal structure is more ordered, which can enhance the interaction between the molecular chains. It may be a key factor hindering photocatalytic degradation.

The relationship between weight loss and the change of morphology, weight-average molecular weight and crystallinity at different hydrothermal temperature and time can

fully prove this conclusion. To be honest, this method does not realize that the entire operation process is carried out at room temperature and ambient pressure and is two-step degradation strategy since the hydrothermal pretreatment is involved. In addition, the limited degradability of the system does not produce satisfactory treatment effects for a large amount of PET-FMPs. Above all, there are still many challenges in exploring the degradation mechanism of PET-FMPs and even plastic waste at present, such as many side reactions and difficulty in in-situ detection of intermediate products. As a result, how to achieve high-efficiency photocatalytic degradation at normal temperature and ambient pressure conditions through a one-step method, and to determine the more detailed and in-depth degradation mechanism of PET-FMPs is the focus of our future work.

Declarations

Conflict of interest The authors declare no competing financial interest.

References

1. Broda J, Przybylo S, Gawlowski A, Grzybowska-Pietras J, Sarna E, Rom M, Laszczak R. Utilisation of textile wastes for the production of geotextiles designed for erosion protection. *J Text I* **2019**;*110*:435.

2. MacDonald S, Pan SW, Hudson D, Tuan F. Chinese domestic textile demand: where they buy does matter. *China Agr Econ Rev* **2013**;*5*:312.

3. Dahlbo H, Aalto K, Eskelinen H, Salmenpera H. Increasing textile circulation-consequences and requirements. *Sustain Pro Consump* **2017**;*9*:44.

4. Shen MC, Zhang YX, Almatrafi E, Hu T, Zhou CY, Song B, Zeng ZT, Zeng GM (2022) Efficient removal of microplastics from wastewater by an electrocoagulation process. Chem Eng J. 428: 131161.

5. Rao WH, Cai CY, Tang JY, Wei YM, Gao CY, Yu L, Ding JD. Coordination insertion mechanism of ring-opening polymerization of lactide catalyzed by stannous octoate. *Chinese J Chem* **2021**;*39*:1965.

6. Zhou DW, Chen JL, Wu J, Yang JP, Wang HP. Biodegradation and catalytic-chemical degradation strategies to mitigate microplastic pollution. Sustain Mater Techno 2021; 28: e00251.

7. Chen JL, Wu J, Wang HP, Yang JP. Research prospect of fibrous microplastics removal in aquatic environment. *J Textile Res* **2021**;*42*:19.

8. Chen F, Zhang Y, Wang Q, Gao MY, Kirby N, Peng ZX, Deng YF, Li MM, Ye L. High T-g polymer insulator yields organic photovoltaic blends with superior thermal stability at 150 degrees C. *Chinese J Chem* **2021**;*39*:2570.

9. Sharma S, Basu S, Shetti NP, Nadagouda MN, Aminabhavi TM (2021) Microplastics in the environment: Occurrence, perils, and eradication. Chem Eng J 408: 127317.

10. Guo Q, Zhou CY, Ma ZB, Ren ZF, Fan HJ, Yang XM. Fundamental processes in surface photocatalysis on TiO$_2$. *Acta Phys-Chim Sin* **2016**;*32*:28.

11. Zhang QL, Hua WQ, Feng JC. A facile strategy to fabricate multi-shape memory polymers with controllable mechanical properties. *Macromol Rapid Commun* **2016**;*37*:1262.

12. Garcia F, de Carvalho AR, Riem-Galliano L, Tudesque L, Albignac M, ter Halle A, Cucherousset J. Stable isotope insights into microplastic contamination within freshwater food webs. *Environ Sci Technol* **2021**;*55*:1024.

13. Lee H, Byun DE, Kim JM, Kwon JH. Desorption modeling of hydrophobic organic chemicals from plastic sheets using experimentally determined diffusion coefficients in plastics. *Mar Pollut Bull* **2018**;*126*:312.

14. Wang F, Shih KM, Li XY. The partition behavior of perfluorooctanesulfonate (PFOS) and perfluorooctanesulfonamide (FOSA) on microplastics. *Chemosphere* **2015**;*119*:841.

15. Ma ZQ, Li BK, Tang RK. Biomineralization: biomimetic synthesis of materials and biomimetic regulation of organisms. *Chinese J Chem* **2021**;*39*:2071.

16. Browne MA, Crump P, Niven SJ, Teuten E, Tonkin A, Galloway T, Thompson R. Accumulation of microplastic on shorelines worldwide: sources and sinks. *Environ Sci Technol* **2021**;*45*:9175.

17. Nava V, Leoni B (2021) A critical review of interactions between microplastics, microalgae and aquatic ecosystem function. Water Res. 188: 116476.

18. Wang TK, Zhang Y, Gu ZC, Cheng W, Lei H, Qin M, Xue B, Wang W, Cao Y. Regulating mechanical properties of polymer-supramolecular double-network hydrogel by supramolecular self-assembling structures. *Chin J Chem* **2021**;*39*:2711.

19. Francesca D, Gennaro G, Roberto A, Emanuela EM, Emilia D, Veronica A, Maurizio A, Mariacristina C. Pectin based finishing to mitigate the impact of microplastics released by polyamide fabrics. *Carbohyd Polym* **2018**;*198*:175.

20. Villa K, Dekanovsky L, Plutnar J, Kosina J, Pumera M. Swarming of perovskite-like Bi(2)WO(6) microrobots destroy textile fibers under visible light. *Adv Funct Mater* **2020**;*30*:2007073.

21. Guo Q, Zhou C, Ma ZB, Yang XM. Fundamentals of TiO$_2$ photocatalysis: concepts, mechanisms, and challenges. *Adv Mater* **2019**;*31*:1901997.

22. Li GW, Wu JN, Fang J, Guo X, Zhu L, Liu F, Zhang MJ, Li YF. A non-fullerene acceptor with chlorinated thienyl conjugated side chains for high-performance polymer solar cells via toluene processing. *Chinese J Chem* **2020**;*38*:697.

23. Rengifo-Herrera JA, Pierzchala K, Sienkiewicz A, Forro L, Kiwi J, Pulgarin C. Abatement of organics and Escherichia coli by N, S co-doped TiO2 under UV and visible light. Implications of the formation of singlet oxygen (O-1(2)) under visible light. Appl Catal B-Environ 2009; 88: 398.

24. Chen WJ, Hsu KC, Fang TH, Lee CI, Chen TH, Hsieh TH. Structural, optical characterization and photocatalytic behavior of Ag/TiO2 nanofibers. *Dig J Nanomater Bios* **2021**;*16*:1227.

25. Li WG, Zuo YJ, Jiang L, Yao DC, Chen ZJ, He GY, Chen HQ. Bi$_2$Ti$_2$O$_7$/TiO$_2$/RGO composite for the simulated sunlight-driven photocatalytic degradation of ciprofloxacin. Mater Chem Phys 2020; 256: 123650.

26. Cai JM, Wu MQ, Wang YT, Zhang H, Meng M, Tian Y, Li XG, Zhang J, Zheng LR, Gong JL. Synergetic enhancement of light

harvesting and charge separation over surface-disorder-engineered TiO$_2$ photonic crystals. *Chem* **2017**;*2*:877.

27. Khan TT, Bari GAKMR, Kang HJ, Lee TG, Park JW, Hwang HJ, Hossain SM, Mun JS, Suzuki N, Fujishima A, Kim JH, Shon HK, Jun YS. Synthesis of N-Doped TiO$_2$ for efficient photocatalytic degradation of atmospheric NO$_x$. Catalysts. 2021; 11: 109.

28. Liu XY, Zhu GL, Wang X, Yuan XT, Lin TQ, Huang FQ. Progress in black titania: a new material for advanced photocatalysis. Adv Energy Mater 2016; 6.

29. Qiu H, Ma XJ, Sun CY, Zhao B, Chen F. Surface oxygen vacancies enriched Pt/TiO$_2$ synthesized with a defect migration strategy for superior photocatalytic activity. Appl Surf Sci 2020; 506: 145021.

30. Wu SY, Wang WJ, Tu WG, Yin SM, Sheng Y, Manuputty MY, Kraft M, Xu R. Premixed stagnation flame synthesized TiO$_2$ nanoparticles with mixed phases for efficient photocatalytic hydrogen generation. *ACS Sustain Chem Eng* **2018**;*6*:14470.

31. Dutta H, Sahu P, Pradhan SK, De M. Microstructure characterization of polymorphic transformed ball-milled anatase TiO$_2$ by Rietveld method. *Mater Chem Phys* **2003**;*77*:153.

32. Hu JF, Qin HW, Sui ZG, Lu HL. Characteristic of mechanically milled TiO$_2$ powders. *Mater Lett* **2002**;*53*:421.

33. Tournier V, Topham CM, Gilles A, David B, Folgoas C, Moya-Leclair E, Kamionka E, Desrousseaux ML, Texier H, Gavalda S, Cot M, Guemard E, Dalibey M, Nomme J, Cioci G, Barbe S, Chateau M, Andre I, Duquesne S, Marty A. An engineered PET depolymerase to break down and recycle plastic bottles. *Nature* **2020**;*580*:216.

34. Zhang HB, Zuo SW, Qiu M, Wang SB, Zhang YF, Zhang J, Lou XW. Direct probing of atomically dispersed Ru species over multi-edged TiO$_2$ for highly efficient photocatalytic hydrogen evolution. Sci Adv 2020; 6: eabb9823.

35. Ma JY, Tan XJ, Zhang QQ, Wang Y, Zhang JL, Wang LZ. Exploring the size effect of Pt nanoparticles on the photocatalytic non-oxidative coupling of methane. *ACS Catal* **2021**;*11*:3352.

36. Huang SS, Ma D, Hu ZJ, He QQ, Zai JT, Chen DY, Sun H, Chen ZW, Qao QQ, Wu MH, Qian XF. Synergistically enhanced electrochemical performance of Ni3S4-PtX (X = Fe, Ni) heteronanorods as heterogeneous catalysts in dye-sensitized solar cells. *ACS Appl Mater Inter* **2017**;*9*:27607.

37. Liu YH, Wu YW, Zhou Y, Wang YT, Yang LY, Li CC. Direct synthesis of urchin-like N-doped TiO$_2$ microstructures with enhanced photocatalytic properties. *T Indian Ceram Soc* **2016**;*75*:155.

38. Esmat M, El-Hosainy H, Tahawy R, Jevasuwan W, Tsunoji N, Fukata N, Ide Y. Nitrogen doping-mediated oxygen vacancies enhancing co-catalyst-free solar photocatalytic H-2 production activity in anatase TiO$_2$ nanosheet assembly. Appl Catal B-Environ. 2021; 285: 119755.

39. Yang YT, Zhang ZS, Fang WH, Fernandez-Alberti S, Long R. Unraveling the quantum dynamics origin of high photocatalytic activity in nitrogen-doped anatase TiO$_2$: time-domain ab initio analysis. *J Mater Chem A* **2020**;*8*:25235.

40. Xu T, Wang M, Wang T. Effects of N doping on the microstructures and optical properties of TiO$_2$. *J Wuhan Univ Technol* **2019**;*34*:55.

41. Ding J, Dai Z, Qin F, Zhao HP, Zhao S, Chen R. Z-scheme BiO$_{1-x}$Br/Bi$_2$O$_2$CO$_3$ photocatalyst with rich oxygen vacancy as electron mediator for highly efficient degradation of antibiotics. *Appl Catal B-Environ* **2017**;*205*:281.

42. Hao L, Huang HW, Zhang YH, Ma TY. Oxygen Vacant Semiconductor Photocatalysts. *Adv Funct Mater* **2021**;*31*:2100919.

43. Hu JS, Li J, Cui JF, An WJ, Liu L, Liang YH, Cui WQ. Surface oxygen vacancies enriched FeOOH/Bi2MoO6 photocatalysis- fenton synergy degradation of organic pollutants. J Hazard Mater 2020; 384: 121399.

44. Sun BJ, Zhou W, Li HZ, Ren LP, Qiao PZ, Xiao F, Wang L, Jiang BJ, Fu HG. Magnetic Fe2O3/mesoporous black TiO2 hollow sphere heterojunctions with wide-spectrum response and magnetic separation. *Appl Catal B-Environ* **2018**;*221*:235.

45. Lin ZY, Liu P, Yan JH, Yang GW. Matching energy levels between TiO$_2$ and alpha-Fe$_2$O$_3$ in a core-shell nanoparticle for visible-light photocatalysis. J Mater Chem A 2015; 3: 14853.

46. Kuang PY, Wang YR, Zhu BC, Xia FJ, Tung CW, Wu JS, Chen HM, Yu JG. Pt single atoms supported on N-doped mesoporous hollow carbon spheres with enhanced electrocatalytic H-2-evolution activity. *Adv Mater* **2021**;*33*:2008599.

47. Wang YR, Zhao JJ, Xiong XQ, Liu SW, Xu YM. Role of Ni2+ ions in TiO$_2$ and Pt/TiO$_2$ photocatalysis for phenol degradation in aqueous suspensions. Appl Catal B-Environ 2019; 258: 117903.

48. Zhou DW, Wu J, Yang JP, Chen Y, Ji P, Wang HP. Research progress of fibrous microplastics and mitigation strategies. *J Textile Res* **2021**;*42*:8.

49. Wakerley DW, Kuehnel MF, Orchard KL, Ly KH, Rosser TE, Reisner E. Solar-driven reforming of lignocellulose to H-2 with a CdS/CdOx photocatalyst. *Nat Energy* **2017**;*2*:17021.

50. Kang J, Zhou L, Duan XG, Sun HQ, Ao ZM, Wang SB. Degradation of cosmetic microplastics via functionalized carbon nanosprings. *Matter* **2019**;*1*:745.

51. Miao F, Liu YF, Gao MM, Yu X, Xiao PW, Wang M, Wang SG, Wang XH. Degradation of polyvinyl chloride microplastics via an electro-Fenton-like system with a TiO$_2$/graphite cathode. J Hazard Mater 2020; 399: 123023.

52. Chen JL, Wu J, Sherrell PC, Chen J, Wang HP, Zhang WX, Yang JP. How to build a microplastics-free environment: strategies for microplastics degradation and plastics recycling. Adv Sci 2022: 2103764.

Publisher's Note Springer Nature remains neutral with regard to jurisdictional claims in published maps and institutional affiliations.

Dawang Zhou is currently pursuing his M.D. degree under the supervision of Prof. Huaping Wang at the College of Materials Science and Engineering, Donghua University. His research interests focus on chemical catalytic degradation of plastics.

Hongxia Luo is currently pursuing her Ph.D. degree under the supervision of Prof. Jianping Yang at the College of Materials Science and Engineering, Donghua University. Her research interests focus on interface design of iron-based materials for electrocatalytic nitrate reduction.

Fangzhou Zhang is currently pursuing her Ph.D. degree under the supervision of Prof. Jianping Yang at the College of Materials Science and Engineering, Donghua University. Her research interests focus on design of fiber structure for electrocatalytic application.

Jing Wu is appointed as a associate researcher and doctoral supervisor in the College of Innovation Center for Textile Science and Technology at Donghua University (China). She received her B.D. degree (2005) at Tianjin University. She then graduated from the Chemistry and Chemical Engineering of Nankai University with M.D. degree (2008) supervised by Professor Zhengming Li. She received the Ph.D. degree (2012) from Eindhoven University of Technology in the Netherlands. Her research interests focus on new environmentally friendly polymer materials, such as bio-based and biodegradable materials.

Jianping Yang is appointed as a Professor and Associate Dean in the College of Materials Science and Engineering at Donghua University (China). He received his B.Sc. degree (2007) at Huazhong University of Science and Technology. His M.Sc. degree (2010) and Ph.D. degree (2013) were received from Fudan University supervised by Professor Dongyuan Zhao. He then worked as a postdoctoral and visiting research fellow at Tongji University, University of Wollongong and Monash University. His research interests focus on interfacial design of functional materials for environmental remediation, electrochemical catalysis, energy conversion and storage.

Huaping Wang is appointed as a researcher and doctoral supervisor in the College of Materials Science and Engineering at Donghua University (China), director of the Key Laboratory (B) of the Ministry of Education for High Performance Fibers and Products, and director of Textile Professional Fiber Materials Teaching Steering Committee, etc. He received his B.D. degree (1986) at the University of Science and Technology of Chengdu. He then graduated from China Textile University with M.D. degree (1989), and received the Ph.D. degree (2001) from Donghua University. His research interests focus on the surface treatment and functional modification of inorganic nanomaterials, surface modification and spinning forming theory and processing technology, etc.